Publication Year	2016
Acceptance in OA@INAF	2020-04-29T11:46:44Z
Title	Searching in the dark: the dark mass content of the Milky Way globular clusters NGC288 and NGC6218
Authors	SOLLIMA, ANTONIO LUIGI; Ferraro, F. R.; Lovisi, L.; Contenta, F.; Vesperini, E.; et al.
DOI	10.1093/mnras/stw1779
Handle	http://hdl.handle.net/20.500.12386/24306
Journal	MONTHLY NOTICES OF THE ROYAL ASTRONOMICAL SOCIETY
Number	462

Monthly Notices
of the
ROYAL ASTRONOMICAL SOCIETY

MNRAS **462,** 1937–1951 (2016)
Advance Access publication 2016 July 25

doi:10.1093/mnras/stw1779

Searching in the dark: the dark mass content of the Milky Way globular clusters NGC288 and NGC6218

A. Sollima,[1,2★] F. R. Ferraro,[2] L. Lovisi,[2] F. Contenta,[3] E. Vesperini,[4] L. Origlia,[1]
E. Lapenna,[2] B. Lanzoni,[2] A. Mucciarelli,[2] E. Dalessandro[2] and C. Pallanca[2]

[1] *INAF Osservatorio Astronomico di Bologna, via Ranzani 1, I-40127 Bologna, Italy*
[2] *Dipartimento di Astronomia, Universitá di Bologna, via Ranzani 1, I-40127 Bologna, Italy*
[3] *Department of Physics, University of Surrey, Guildford GU2 7XH, UK*
[4] *Department of Astronomy, Indiana University, Bloomington, IN 47405, USA*

Accepted 2016 July 18. Received 2016 July 18; in original form 2016 May 3

ABSTRACT

We present an observational estimate of the fraction and distribution of dark mass in the innermost region of the two Galactic globular clusters NGC 6218 (M12) and NGC 288. Such an assessment has been made by comparing the dynamical and luminous mass profiles derived from an accurate analysis of the most extensive spectroscopic and photometric surveys performed on these stellar systems. We find that non-luminous matter constitutes more than 60 per cent of the total mass in the region probed by our data ($R < 1.6$ arcmin $\sim r_{\rm h}$) in both clusters. We have carefully analysed the effects of binaries and tidal heating on our estimate and ruled out the possibility that our result is a spurious consequence of these effects. The dark component appears to be more concentrated than the most massive stars suggesting that it is likely composed of dark remnants segregated in the cluster core.

Key words: methods: data analysis – techniques: radial velocities – stars: kinematics and dynamics – stars: luminosity function, mass function – stars: Population II – globular clusters: individual: NGC6218, NGC288.

1 INTRODUCTION

The relative contribution of luminous and dark matter (DM) to the overall mass budget of stellar systems contains crucial information on their nature, origin and evolution. According to the Λ cold dark matter cosmological paradigm, the structures in the Universe formed at high redshift through a hierarchical assembly of small fragments of non-baryonic matter (White & Rees 1978). Galaxies of all morphological types are expected to form within these fragments being nowdays embedded in DM haloes. This evidence comes from the discrepancy between the mass estimated for these stellar systems using the kinematics of their stars and their luminosities as tracers. In particular, the mass-to-light (M/L) ratios measured for these stellar systems range from 5 (for dwarf elliptical galaxies) to >1000 (for ultrafaint dwarf spheroidals; Tollerud et al. 2011) i.e. several times larger than those predicted by population synthesis models ($1.5 < M/L < 2.5$; Bruzual & Charlot 2003).

Globular clusters (GCs) appears to stand-out from this scenario. Indeed, at odds with other DM dominated stellar systems populating contiguous regions of the luminosity-effective radius plane (Tolstoy, Hill & Tosi 2009), they have low M/L ratios consistent with the hypothesis they are deprived of DM (McLaughlin & van der Marel 2005; Strader, Caldwell & Seth 2011). This difference might suggest a different formation scenario for these stellar systems which could form in collapsing DM-free gas clouds (see e.g. Kruijssen 2015). For this reason, the M/L ratios of GCs are often used as a reference for stellar population studies and to validate the prediction of population synthesis models. On the other hand, low-mass DM haloes surrounding GCs progenitors are hypothesized by some model of GC formation (Peebles 1984). These haloes could be later stripped by the tidal interaction with the host galaxy leaving only minimal imprints in the structural and kinematical properties of present-day GCs (Mashchenko & Sills 2005). Observational claims of the possible existence of DM dominated GCs in the giant elliptical NGC 5128 have been recently put forward by Taylor et al. (2015).

Non-baryonic DM is not the only invisible matter contained in stellar systems. Indeed, the final outcome of the stellar evolution process of stars with different masses is represented by remnants (white dwarfs – WFs, neutron stars – NSs – and black holes – BHs) whose luminosities are comparable or even several orders of magnitude smaller than those of the least luminous main-sequence (MS) stars. The estimate of the mass enclosed in dark remnants in a GC is complicated by the interplay between stellar and dynamical evolution in these stellar systems and by the uncertainties in their

---

[★] E-mail: antonio.sollima@oabo.inaf.it

Published by Oxford University Press on behalf of the Royal Astronomical Society

formation process (for a comprehensive discussion see Heggie & Hut 1996).

Indeed, both NSs and BHs are the compact remnants of massive ($M > 8\,\mathrm{M}_{\odot}$) stars after their explosion as SNe II. The off-centre onset of the explosive mechanism can transmit to the remnant a velocity kick often exceeding the cluster escape speed thus leading to its ejection outside the cluster (Drukier 1996; Moody & Sigurdsson 2009). Moreover, the large mass contrast of BHs with respect to the mean cluster mass lead to a quick collapse of the BH population forming a dynamically decoupled subsystem in the central part of the cluster (Spitzer 1969). Scattering between multiple BHs leads to a prompt ejection of these objects. For the above mentioned reasons, it was initially suggested that GCs should be deprived of BHs (Kulkarni, Hut & McMillan 1993; Sigurdsson & Hernquist 1993). However recent observational studies (see e.g. Strader et al. 2012; Chomiuk et al. 2013; Miller-Jones et al. 2015) have provided evidence of the possible presence of stellar mass BHs in a number of GCs and several theoretical studies (see e.g. Banerjee & Kroupa 2011; Breen & Heggie 2013; Morscher et al. 2013, 2015; Sippel & Hurley 2013; Heggie & Giersz 2014) have found that GCs might indeed still host a non-negligible fraction of these compact objects. On the other hand, the large fraction of X-ray binaries and pulsars per unit mass in GCs (up to a factor 100 larger than that estimated in the Galactic field; Clark 1975; Grindlay & Bailyn 1988) indicates that a certain number of these objects must be present in these stellar systems.

WDs are the natural outcome of the evolution of low-/intermediate-mass ($M < 8\,\mathrm{M}_{\odot}$) stars after the expulsion of their envelopes occurring at the end of their asymptotic giant branch phase. As a consequence of the long lifetimes of WD progenitors and the typical negative slope of the initial mass function (MF; Kroupa 2001; Bastian, Covey & Meyer 2010) the fraction of WDs steadily increases during the cluster lifetime making them a significant contributor to the mass budget of a GC in the last stages of its evolution (Vesperini & Heggie 1997; Baumgardt & Makino 2003). Because of the particular form of the initial–final mass relation of low-mass stars (Kalirai et al. 2008), the mass spectrum of these objects is expected to be peaked at $M \sim 0.5\,\mathrm{M}_{\odot}$ i.e. only slightly larger than the present-day mean stellar mass ($\sim 0.4\,\mathrm{M}_{\odot}$) and significantly smaller than the typical turn-off mass in a GC ($\sim 0.8\,\mathrm{M}_{\odot}$). So, at odds with NSs and BHs occupying always the high tail of the mass distribution of stellar objects, stars evolving into WDs change their ranking in mass within the whole GC stellar population during their lifetimes. Consequently, two-body relaxation is expected to produce a progressive migration of WDs from the centre, where their massive progenitors sunk, towards the outer regions where stars with smaller masses are preferentially located. Observational evidence of this phenomenon seems to be provided by the analysis of the radial distribution of WDs in different regions of the cooling sequence in 47 Tucanae (Heyl et al. 2015). The interaction of a GC with the tidal field of its host galaxy further complicate the prediction of the retention fraction of dark remnants. Indeed, the ever continuing injections of kinetic energy favours the evaporation of the kinematically hottest (mainly low-mass) stars, while massive objects (like NSs, BHs and massive WD progenitors) are preferentially retained. *N*-body simulations indicate that the actual fraction of retained remnants has deep implications in the dynamical evolution of GCs (Contenta, Varri & Heggie 2015) and in their present-day M/L ratios (Lützgendorf, Baumgardt & Kruijssen 2013).

In this context, many observational analyses aimed at investigating the dark content in GCs have been conducted in the past years by comparing the M/L ratios estimated from stars kinematics and those predicted by stellar population synthesis models (Richer & Fahlman 1989; Meylan & Mayor 1991; Leonard, Richer & Fahlman 1992; Piatek et al. 1994; Dirsch & Richtler 1995; Ibata et al. 2013; Lützgendorf et al. 2013; Kamann et al. 2014). One of the main drawbacks of this approach resides in the choice of the uncertain parameters affecting the M/L like the present-day MF and the retention fraction of dark remnants (Shanahan & Gieles 2015).

In Sollima, Bellazzini & Lee (2012), we determined the dynamical and luminous masses of a sample of six Galactic GCs by fitting simultaneously their luminosity functions and their line-of-sight (LOS) velocity dispersion profiles with multimass analytical models leaving the present-day MF as a free parameter and making an assumption on the dark remnants retention fraction. From this study, we found that the derived stellar masses were systematically smaller than the dynamical ones by ∼40 per cent. Although many hypotheses were put forward, the most favoured interpretation linked such a discrepancy to a fraction of retained dark remnants larger than expected. Unfortunately, the robustness of the obtained result relies on the ability of the adopted specific model in reproducing the actual degree of mass segregation of the analysed clusters. In particular, both the luminous and the dynamical masses of the best-fitting model were constrained by observables measured in the cluster core, a region where mass segregation effects are maximized and where only a small fraction of the cluster mass is contained, and then extrapolated to the whole cluster (see Sollima et al. 2015). Moreover, the approach adopted in that work did not allow us to obtain information on the radial distribution of the dark mass across the cluster, therefore complicating any interpretation on its nature.

In this paper, we present the result of a model-independent analysis of the most extensive photometric and spectroscopic data sets available in the literature for two Galactic GCs, namely NGC 288 and NGC 6218 (M12) with the aim of deriving their dark mass content and radial distribution. These objects are two well-studied GCs located in the Southern hemisphere which are particularly suited for this kind of studies. Both clusters are indeed relatively close ($d <$ 9 kpc) and characterized by a small central projected density ($\Sigma_V >$ 18 mag arcsec^{-2}; Harris 1996, 2010 edition) and for this reason it is possible to sample their luminosity function and velocity dispersion profiles through photometric and spectroscopic surveys even within their cores with no significant crowding problems. In Section 2, we describe the observational data set used in the analysis and the data reduction techniques. In Section 3, the methods to derive luminous and dynamical mass profiles for the two target clusters are described. The fractions of dark mass as a function of the projected distance from the clusters' centres are shown in Section 4. The comparison with the prediction of *N*-body simulations and analytical models is performed in Section 5 to quantify the expected effect of a sizable population of dark remnants. We summarize and discuss our results in Section 6.

2 OBSERVATIONAL DATA

The analysis performed here is based on both photometric and spectroscopic data sets. The main photometric data base is constituted by the set of publicly available deep photometric catalogues of the 'globular cluster treasury project' (Sarajedini et al. 2007). It consists of high-resolution *Hubble Space Telescope* (*HST*) images secured with the Advanced Camera for Surveys (ACS) Wide Field Channel through the *F*606*W* and *F*814*W* filters. The field of view of the camera (202 arcsec × 202 arcsec) is centred on the cluster's centre with a dithering pattern to cover the gap between the two chips,

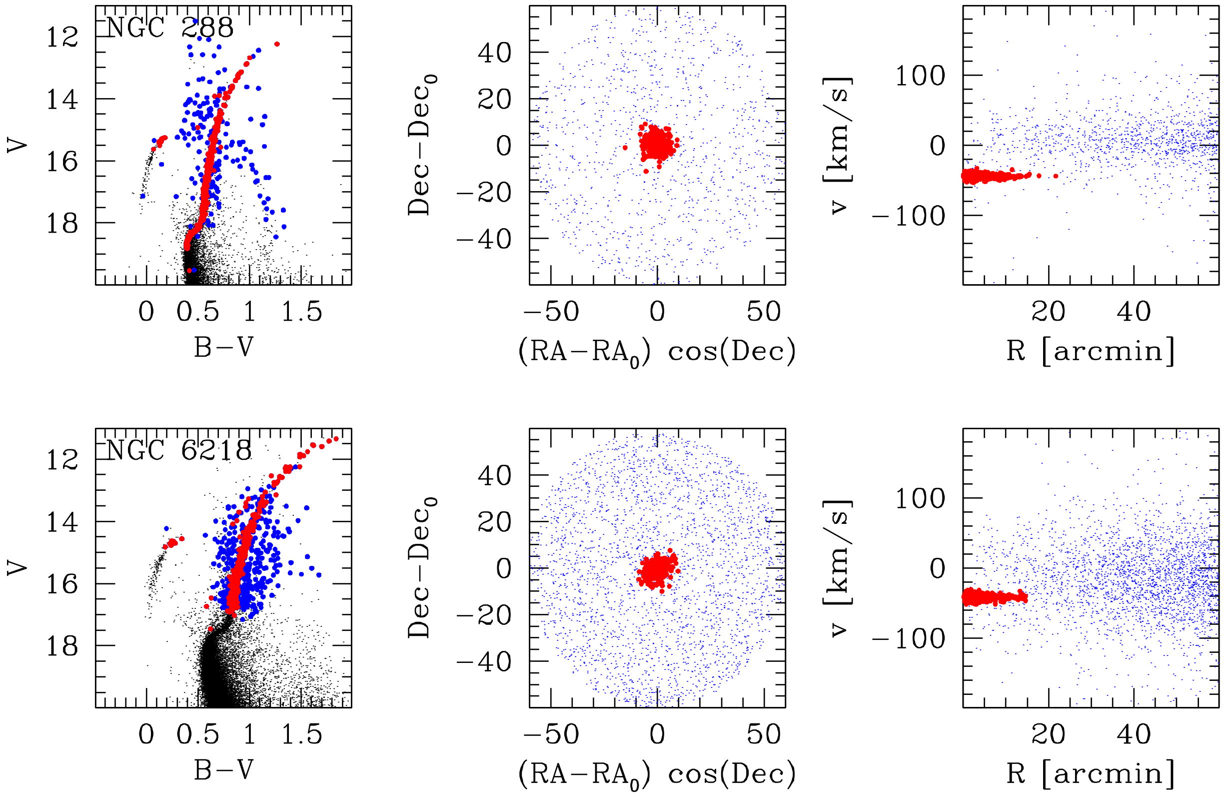

Figure 1. Left-hand panels: WFI CMDs of the two analysed clusters (black dots). Middle panels: spatial location of our spectroscopic targets. Right-hand panels: radial velocities as a function of the distance from the cluster centre. In all panels, stars with measured radial velocities and bona-fide cluster members (see Section 3.2) are marked with blue and red dots (dark grey and black in the printed version of the paper), respectively. Top and bottom panels refer to NGC 288 and NGC 6218, respectively.

allowing a full coverage of the core of both the GCs considered in our analysis. This survey provides deep colour–magnitude diagrams (CMDs) reaching the faint MS of the target clusters down to the hydrogen burning limit (at $M_V \sim 10.7$) with a signal-to-noise ratio S/N>10. The results of artificial star experiments are also available to allow an accurate estimate of the completeness level and photometric errors. A detailed description of the photometric reduction, astrometry, and artificial star experiments can be found in Anderson et al. (2008). Auxiliary wide-field photometric data are needed in our work to determine the radial density profile of the two analysed clusters across their entire extent. For this purpose, we analysed a set of images collected with the Wide Field Imager (WFI) mounted on the 2.2 m telescope of the European Southern Observatory (ESO; La Silla, Chile). The WFI covers a total field of view of 34 arcmin × 33 arcmin consisting of eight 2048 × 4096 EEV-CCDs with a pixel size of 0.238 arcsec^{-1} pixel^{-1}. Observations were carried out in two photometric nights on 2001 October and 2002 June within the observing programmes 68.D-0212(A, PI: Ferraro) and 69.D-0582(A, PI: Ortolani) for NGC 288 and NGC 6218, respectively, both aimed at the characterization of the stellar populations of a sample of Galactic GCs. They consist of a set of *B* and *V* images with a dithering pattern to cover the gaps between the CCDs. One shallow and three deep exposures have been secured for each cluster in both passbands to avoid saturation of the bright red giant branch (RGB) stars and, at the same time, sample the faint MS stars with a good signal-to-noise ratio. The photometric reduction of both data sets has been performed using the DAOPHOT/ALLFRAME point spread function-fitting routine (Stetson 1994). We performed the source detection on the stack of all images while the photometric analysis was performed independently on each image. Only stars detected in two out of three long exposures or in the short ones have been included in the final catalogue. We used the most isolated and brightest stars in the field to link the aperture magnitudes to the instrumental ones. Instrumental *V* magnitudes have been transformed into the ACS *F606W* system using a first-order linear relation obtained by comparing the stars in common between the two data sets. The final catalogues have been astrometrically calibrated through a cross-correlation with the 2MASS catalogue (Skrutskie et al. 2006). The astrometric solution has a typical standard deviation of 200 mas. The final WFI CMDs sample the entire evolved population of both clusters and the MS down to $V \sim 23$ i.e. ∼4.5 mag below the turn-off (see Fig. 1). Artificial star experiments show that the completeness at distance >1.6 arcmin (approximately the ACS field of view) is >90 per cent for $V < 20$.

The radial velocity data base has been assembled using spectra observed in different spectroscopic campaign, in particular:

(i) the bulk of our data set within the clusters' tidal radii comes from the analysis of spectra secured within the large programme 193.D-0232 (PI: Ferraro) aimed at probing the internal dynamics of a sample of 30 Galactic GCs. Observations have been performed with the Fibre Large Array Multi-Element Spectrograph (FLAMES; Pasquini et al. 2002) at the ESO Very Large Telescope used in GIRAFFE mode, using the high-resolution ($R \sim 18\,000$) grating HR21 (8484–9001 Å). Three and seven pointings have been performed in NGC 288 and NGC 6218, respectively, reaching an S/N of 50–300 pixel^{-1}, depending on the star magnitude.

Table 1. Summary of the adopted radial velocity data sets.

Observing programme	PI	NGC 288 FLAMES setups	# of targets	# of *bona-fide* targets
071.D-0131(A)	Moheler	LR1/LR2/LR3	20	17
073.D-0211(A)	Carretta	HR11/HR13	117	111
074.A-0508(A)	Drinkwater	LR2/LR4	87	57
075.D-0043(A)	Carraro	HR9	175	161
087.D-0276(A)	D'Orazi	HR15/HR19	78	75
088.B-0403(A)	Lucatello	HR9	88	84
193.D-0232(D)	Ferraro	HR21	174	162
AAO	Lane		1237	152
		NGC 6218		
073.D-0211(A)	Carretta	HR11/HR13	92	82
087.D-0276(A)	D'Orazi	HR15	76	73
193.B-0936(I)	Gilmore	HR10	108	86
193.D-0232(B)	Ferraro	HR21	385	321
AAO	Lane		2937	317

(ii) All the FLAMES spectra available at the ESO archive for the two target clusters have been retrieved and analysed using the same technique adopted for the above described data set. They consist of surveys of RGB stars observed with different setups and resolutions collected in the last 13 yr. A summary of the data bases used in this work is given in Table 1.

(iii) The above data sets have been complemented with the radial velocity data base by Lane et al. (2010, 2011) performed using the multifibre spectrograph mounted at the Anglo-Australian Telescope AAOmega (AAO) which covers a wide area around the target clusters up to a distance of 1° from the clusters' centres, sampling the whole radial extent of the clusters and the surrounding field population. Spectra were observed with the 1700D and 1500V gratings on the red and blue arms, respectively. With this configuration, spectra covering the Ca II triplet region (8340–8840 Å) and the interval containing iron and magnesium lines around ∼5200 Å were obtained with a resolution of $R = 10\,000$ and $R = 3700$ for the red and blue arms, respectively. A detailed description of the reduction procedure and radial velocity estimates can be found in Lane et al. (2010, 2011). For this work, we adopted the radial velocities extracted with the RAVE pipeline since they provide a better estimate of the radial velocity uncertainty when compared with the available high-resolution spectroscopic studies (see Bellazzini et al. 2012).

Raw FLAMES data have been reduced with the GIRAFFE ESO Base-Line Data Reduction Software v2.14.2 (BLDRS) which includes bias subtraction, flat-field correction, cosmic rays removal, wavelength calibration and one-dimensional spectra extraction. The spectra acquired with the fibres dedicated to sky observations in each exposure have been averaged to obtain a mean sky spectrum and subtracted from the object spectra by taking into account the different fibre transmission. The spectra have been then continuum-normalized with fifth-degree Chebyshev polynomials using the IRAF task *continuum*. Radial velocities have been derived through Fourier cross-correlation, using the *fxcor* task in the radial velocity IRAF package. The spectrum of each object has been correlated with a high S/N solar spectrum observed with FLAMES with the same instrumental setup. All spectra have been corrected for heliocentric velocity. For the subset of stars that were repeatedly observed within each data set radial velocities have been averaged and the corresponding errors on the mean of repeated measures have been assigned as their corresponding uncertainties. The errors determined from more than three measures have been then compared with the formal errors provided by the cross-correlation algorithm. We find a scaling factor of $\sigma_{\rm rms}/\sigma_{\rm Xcorr} = 0.9$ between these two estimates which has been used to convert the uncertainties of radial velocities measured in <3 exposures to the same scale of other measures. Radial velocities from different data sets have been reported to a homogenous reference system using as reference the AAO sample which provides a significant (>20) overlap with the other data sets. Radial velocities measured in multiple data sets have been compared to estimate the occurrence of binarity: as a selection criterion, we flagged as binaries those stars whose probabilities that the observed scatter is due to statistical fluctuations (estimated through a χ^2 test) is below 1 per cent (see Lucatello et al. 2005). Of the 193 and 295 stars measured in multiple data sets, we found 15 and 20 binaries in NGC 288 and NGC 6218, respectively, in agreement with the binary fractions measured in these GCs by many authors with different techniques (Bellazzini et al. 2002; Sollima et al. 2007; Milone et al. 2012; Lucatello et al. 2015). Radial velocities of single stars measured in different data sets have been then averaged, while binaries have been excluded from the following analysis. The effect of the residual contamination from binaries in single-epoch data sets is discussed in Section 4.1. The final data sets consist of 1586 and 3188 radial velocities in NGC 288 and NGC 6218, respectively, sampling mainly RGB stars plus some asymptotic giant and red horizontal branch (HB) star across the entire radial extent of both clusters (see Fig. 1). The radial velocity uncertainties are generally in the range $0.1 < \delta_v/\mathrm{km\,s^{-1}} < 1.2$ with a mean value of $\langle\delta_v\rangle = 0.6\,\mathrm{km\,s^{-1}}$.

3 METHOD

The fraction and distribution of the dark mass in the two analysed GCs have been determined by comparing the mass profile derived by summing the masses of individual stars estimated from the ACS CMD (the 'luminous mass profile') and that estimated through the Jeans analysis of the spectroscopic data set (the 'dynamical mass profile'). In the next sections, we describe the techniques used to derive these profiles.

3.1 Luminous mass profiles

The deep CMDs provided by the 'ACS GC treasury project' sample the entire unevolved stellar populations of the analysed clusters reaching the hydrogen burning limit with a completeness >90 per cent. The only objects excluded from this sample are the dark remnants whose luminosities fall below the detection limit of ACS observations. GC stars occupy different regions of the CMD according to their evolutionary stages and masses, so an estimate of their masses can be made through the comparison with suitable theoretical isochrones. We adopted the theoretical isochrones by Dotter et al. (2007) with appropriate ages and metallicity which have been converted into the observational colour–magnitude plane assuming the distance moduli and reddening $(m - M)_0 = 14.83$; $E(B - V) = 0.01$ for NGC 288 and $(m - M)_0 = 13.46$; $E(B - V) = 0.19$ for NGC 6218 (Dotter et al. 2010; Sollima et al. 2012).

In principle, some contamination from fore/background field stars can affect star counts at various magnitude levels. However, because of the relatively high Galactic latitude of the two target clusters ($b < -25°$), the density of field stars within the cluster core is several orders of magnitude smaller than that of the GC population: a comparison with the Galactic model of Robin et al. (2003) indicates that less than 0.1 per cent of the stars within the selection boxes adopted in our analysis are expected to be field contaminants in both the analysed GCs. For this reason, we do not apply any correction for this effect in our analysis.

The effect of unresolved binaries and photometric errors can have a critical impact by spreading out stars far from their original location in the CMD, making difficult to assign them a proper mass. The emerging flux from an unresolved binary star is given by the sum of the fluxes of the two component. According to the mass ratio (q) of the binary components the star will move in the CMD towards brighter magnitudes and redder colours with respect to a single star with a mass equal to the mass of the primary component of the binary. Because of photometric errors, the positions in the CMD of binaries and single stars partially overlap in the region close to the MS locus where both low-q binaries and single stars reside. Moreover, the same effect that increases the binaries magnitudes occurs as a result of chance superpositions between single stars, which can occur in the dense central region of GCs. Although it is not possible to unambiguously distinguish binaries and single stars across the entire CMD, we adopt a statistical classification of cluster members. For this purpose, the field of view of the ACS data has been divided in 16 annular concentric regions with both width and separation of 0.1 arcmin. For each region, a synthetic CMD has been simulated by randomly extracting masses from a power-law MF and deriving the corresponding *F*606*W* and *F*814*W* magnitudes by interpolating through the adopted isochrone. A population of binaries has been also simulated by associating to a fraction of stars a secondary component with a mass randomly extracted from a flat mass-ratios distribution (Milone et al. 2012). The fluxes of the two components have been then summed in both passbands to derive their corresponding magnitudes and colour. For each single and binary system, a synthetic star in the same radial range and with magnitudes within 0.25 mag has been extracted from the library of artificial stars and, if recovered, its output magnitude and colour have been adopted to construct the synthetic CMD. In this way, the effect of photometric errors, blending and completeness at the different distances from the cluster centre are properly taken into account. In each radial bin, the MF slope and the binary fraction[1] have been tuned to reproduce the number counts in nine regions of the *F*814*W*-(*F*606*W*-*F*814*W*) CMD defined as follows: eight *F*814*W* magnitude intervals corresponding to equal-mass intervals and including all stars with colours within three times the photometric error corresponding to their magnitudes, and a region including the bulk of the binary population with high-mass ratios ($q > 0.5$). This last region is delimited in magnitudes by the loci of binaries with primary star mass $M_1 = 0.45\,\mathrm{M}_\odot$ (faint boundary) and $M_1 = 0.75\,\mathrm{M}_\odot$ (bright boundary), and in colour by the MS ridge line (blue boundary) and the equal-mass binary sequence (red boundary), both redshifted by three times the photometric error (see Fig. 2). A synthetic HB has been also simulated for each cluster using the tracks by Dotter et al. (2007), tuning the mean mass and mass dispersion along the HB to reproduce the observed HB morphology. As a final step, we associated with each observed star the mass of the closest synthetic object in the simulated CMD. We associated with each observed star a completeness factor (c_i) defined as the fraction of recovered artificial stars[2] with input magnitudes

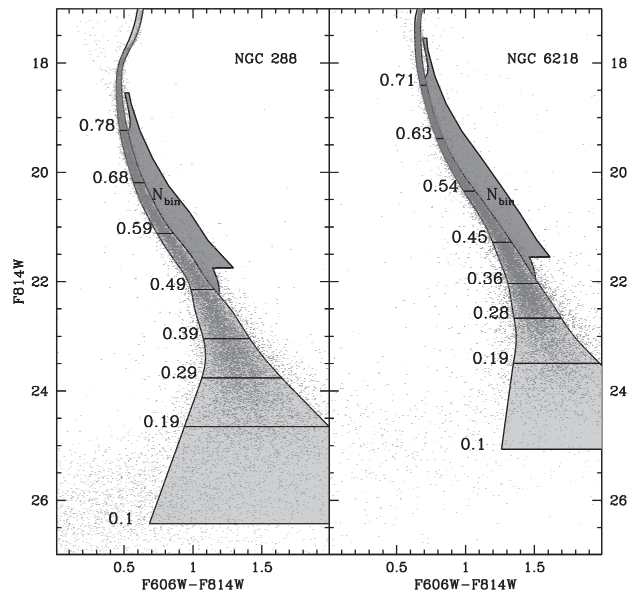

Figure 2. Selection boxes adopted for the population of single stars and binaries (Nbin) of NGC 288 (left-hand panel) and NGC 6218 (right-hand panel). The *F*814*W*-(*F*606*W*-*F*814*W*) CMD is overplotted. The stellar masses at different magnitude levels are indicated in both panels.

in both bands within 0.25 mag and distance from the cluster centre within 0.05 arcmin from those of the corresponding observed star. The cumulative radial distribution of luminous mass has been then derived by summing the completeness-weighted masses of all stars within a given projected distance

$$M_{\mathrm{lum}}(R) = \sum_{d_i < R} \frac{m_i}{c_i}. \quad (1)$$

Following the above procedure, the luminous mass enclosed within a projected distance equal to the extent of the ACS field of view (1.6 arcmin) turns out to be $9.3 \pm 0.9 \times 10^3\,\mathrm{M}_\odot$ and $1.2 \pm 0.1 \times 10^4\,\mathrm{M}_\odot$ for NGC 288 and NGC 6218, respectively. As expected, in both clusters the evolved stellar populations (subgiant branch, RGB, HB and asympthotic giant branch) contribute to only a small fraction of the cluster mass (6 and 8 per cent in NGC 288 and NGC 6218, respectively).

3.2 Dynamical mass profiles

The dynamical mass profile $M_{\mathrm{dyn}}(R)$ has been derived by solving the Jeans equation in spherical coordinates

$$\frac{1}{\rho_*}\frac{\mathrm{d}\rho_*\sigma_{r,*}^2}{\mathrm{d}r} + 2\beta\frac{\sigma_{r,*}^2}{r} = -\frac{GM(r)}{r^2}, \quad (2)$$

where ρ_* and $\sigma_{r,*}$ are the 3D mass density and the radial component of the velocity dispersion of a tracer population at the distance r from the cluster centre, $\beta \equiv 1 - \sigma_{t,*}/2\sigma_{r,*}$ is the anisotropy profile and G is the Newton constant. The Jeans equation follows directly from the collisionless Boltzmann equation and it is based on the concept that any given population is in hydrostatic equilibrium within the cluster potential. This statement holds even if the potential is not completely generated by the considered population (like in the case of a mass-segregated stellar system or a DM dominated galaxy). The advantage of the above equation is that it links two observable quantities (density and velocity dispersion profiles) of an arbitrary sample population to a global quantity (the mass profile generating

---

[1] Note that because of the choice of a fixed mass-ratio distribution for binaries, the binary fraction and the MF slope do not constitute a degenerate space of solutions.

[2] An artificial star has been considered recovered if its input and output magnitudes differ by less than 2.5 log(2) (∼0.75) mag in both *F*606*W* and *F*814*W* magnitudes.

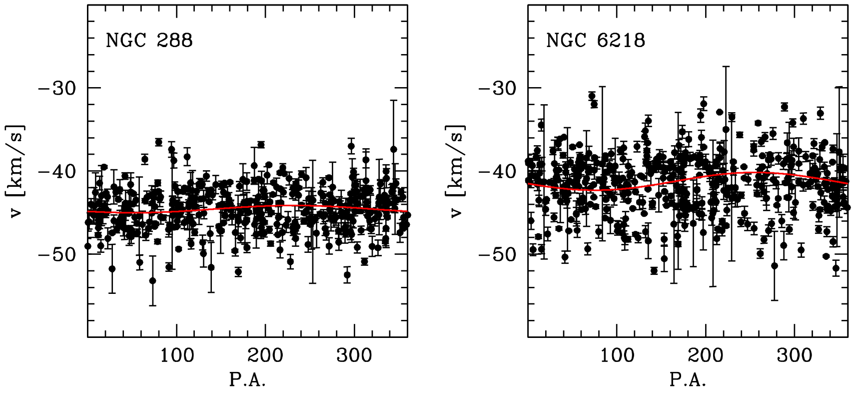

Figure 3. Radial velocity of the *bona-fide sample* stars of NGC 288 (left-hand panel) and NGC 6218 (right-hand panel) as a function of the position angle. The best-fitting sinusoidal trends are marked with solid lines.

the gravitational potential). Any spherical pressure-supported system at equilibrium must obey to the above equation, which allows us to derive the dynamical mass profile once the 3D density, velocity dispersion and anisotropy profiles of a tracer population are known.

The observed projected density profiles have been constructed from both ACS and WFI photometric data by dividing the number of stars brighter than a threshold magnitude and contained in circular concentric annuli by the annulus area. The threshold magnitude has been chosen to include MS and RGB stars with masses $M > 0.875\,M_{\rm tip} + 0.01$, where $M_{\rm tip}$ is the mass at the tip of the RGB extracted from the best-fitted isochrone (see Section 3.1). This ensures to sample the density profile of stars with similar masses of those for which radial velocities are available, thus minimizing variations induced by two-body relaxation while still guaranteeing a good statistics to sample the outskirts of both clusters. Only stars within three times the colour dispersion around the MS/RGB mean ridge line have been used to avoid contamination from Galactic field stars which could be particularly severe in the outermost cluster region. WFI data have been used at distances >1.6 arcmin while ACS data have been used to sample the density profile in the innermost region of the clusters where crowding might affect completeness in ground-based data. The two profiles have been normalized using stars in common in the outermost bin of ACS data. Star counts have been corrected for incompleteness using corrections derived from artificial star experiments. The resulting profiles are consistent with those already published by other authors (Trager, King & Djorgovski 1995; Miocchi et al. 2013). Angular distances of both photometric and spectroscopic targets have been converted in physical units adopting the distance moduli and reddening corrections reported in Section 3.1.

The analysis of radial velocities has been performed on a *bona-fide sample* defined selecting stars with (i) radial velocities within $5\langle\sigma_{\rm LOS}\rangle$ from the mean systemic velocity, (ii) distance from the clusters' centres smaller than the cutoff radius apparent in the density profile ($r_{\rm t}$; at 32 arcmin and 15 arcmin for NGC 288 and NGC 6218, respectively) and (iii) location in the CMD within five times the colour dispersion about the MS/RGB mean ridge line. The mean systemic velocity and dispersion ($\bar{v}$ and $\langle\sigma_{LOS}\rangle$) have been derived by maximizing the loglikelihood

$$l = \sum_i ln \int_{-\infty}^{+\infty} \frac{\exp\left[-\frac{(v'-\bar{v})^2}{2\langle\sigma_{\rm LOS}\rangle^2} - \frac{(v_i-v')^2}{2\delta_i^2}\right]}{2\pi\langle\sigma_{\rm LOS}\rangle\delta_i}{\rm d}v'$$

$$= -\frac{1}{2}\sum_i \left(\frac{(v_i-\bar{v})^2}{\langle\sigma_{\rm LOS}\rangle^2+\delta_i^2} + ln\left[2\pi\left(\langle\sigma_{\rm LOS}\rangle^2+\delta_i^2\right)\right]\right), \qquad (3)$$

where v_i and δ_i are the velocity of the *i*th star and its associated uncertainty. The derived values of $\bar{v}$ for the two clusters are -44.58 ± 0.12 and $-41.24 \pm 0.15\,{\rm km\,s^{-1}}$ for NGC 288 and NGC 6218, respectively. By applying the above selection criteria, the *bona-fide samples* contain 405 and 449 stars for NGC 288 and NGC 6218, respectively.

In principle, systemic rotation affects the dynamical equilibrium of a stellar system requiring additional terms to be added to equation (2). In Fig. 3, the radial velocities of the *bona-fide sample* as a function of the position angle are shown for the two analysed clusters. The distributions appear homogeneous with no apparent trends. A fit with sinusoidal curves indicate maximum rotation amplitudes of $v_{\rm rot}\sin i = 0.43 \pm 0.48\,{\rm km\,s^{-1}}$ for NGC 288 and $v_{\rm rot}\sin i = 1.07 \pm 0.72\,{\rm km\,s^{-1}}$ for NGC 6218, consistent in both cases with no significant rotation along the LOS (see also Bellazzini et al. 2012). For this reason rotation terms in the Jeans equation have been neglected for both clusters.

In the literature, many groups inverted the Jeans equation adopting smoothed density and velocity dispersion profiles (Gebhardt & Fischer 1995; Ibata et al. 2013; Lützgendorf et al. 2013; Watkins et al. 2015b). There are however two drawbacks in this approach: (i) according to equation (2), the derived mass profile depends on the derivatives of the density and velocity dispersion profiles. So, any fluctuation due to Poisson noise in observational data produces an unphysical behaviour of the derived mass profile; (ii) a given $M(r)$ profile can be a solution of the Jeans equation even if it provides a non-physically meaningful representation of the system i.e. corresponding to a distribution function which is negative somewhere in the energy domain. To overcome the above issues, we fit both the projected density and LOS velocity dispersion profiles of our tracer population with parametric analytical functions, by exploring only the portion of the parameter space providing physically meaningful solutions (i.e. those corresponding to positive distribution functions; see Appendix).

A particularly convenient choice is to model the derived 3D density and square velocity dispersion profiles with a sum of Gaussian functions with different dispersions (Cappellari 2002)

$$\rho_* = \sum_j \mu_j \exp\left(-\frac{r^2}{2s_j^2}\right)$$

$$\sigma_{r,*}^2 = \sum_j k_j \exp\left(-\frac{r^2}{2s_j^2}\right) \qquad (4)$$

so that their radial derivatives can always be expressed as sums of functions with the same coefficients

$$\frac{\mathrm{d}^n \rho_*}{\mathrm{d}r^n} = \sum_j \mu_j \frac{\mathrm{d}^n}{\mathrm{d}r^n} \exp\left(-\frac{r^2}{2s_j^2}\right)$$
$$\frac{\mathrm{d}^n \sigma_{r,*}^2}{\mathrm{d}r^n} = \sum_j k_j \frac{\mathrm{d}^n}{\mathrm{d}r^n} \exp\left(-\frac{r^2}{2s_j^2}\right). \tag{5}$$

The 3D mass and global density profiles can be then derived from equation (2), (4) and (5) as

$$M(r) = -\frac{\sigma_{r,*}^2 r^2}{G}\left(\frac{1}{\rho_*}\frac{\mathrm{d}\rho_*}{\mathrm{d}r} + \frac{1}{\sigma_{r,*}^2}\frac{\mathrm{d}\sigma_{r,*}^2}{\mathrm{d}r} + \frac{2\beta}{r}\right)$$
$$\rho(r) = \frac{1}{4\pi r^2}\frac{\mathrm{d}M}{\mathrm{d}r}. \tag{6}$$

In the same way, high-order derivatives of density can be also analytically calculated from the above equation. The advantage of this choice is twofold: first, once the coefficients μ_j and k_j are determined, the corresponding projected density and LOS velocity dispersion of the tracer population can be directly computed as

$$\Gamma(R) = \sum_j \mu_j \int_R^{+\infty} \frac{r\ \mathrm{e}^{r^2/2s_j^2}}{\sqrt{r^2 - R^2}}\mathrm{d}r$$
$$\sigma_{\mathrm{LOS}}^2(R) = \frac{1}{\Gamma(R)}\sum_j k_j \int_R^{+\infty} \rho_* \mathrm{e}^{r^2/2s_j^2}\frac{r^2 - \beta R^2}{r\sqrt{r^2 - R^2}}\mathrm{d}r, \tag{7}$$

respectively. Secondly, the derived 3D density and velocity dispersion profiles are already smooth functions of radius and their integrals and derivatives can be quickly computed analytically. The Gaussian widths s_j (the same for both the density and velocity dispersion) have been chosen to increase in logarithmic steps of 0.1 from 1 pc to the cut radius. The μ_j coefficients were first derived through a χ^2 minimization between the observed projected density profile of tracers and that derived through equation (4) and (7). Then, the space of k_j coefficients has been sampled with a Metropolis–Hasting Markov Chain Monte Carlo (MCMC) technique to reproduce the distribution of velocities in the $v - R$ plane. Note that residual contamination from fore/background field stars can be present in the *bona-fide sample*, in particular in the outer portions of the clusters where the density of the tracer population falls below the density of field contaminants. To account for this effect, we modelled the population of field stars with a Gaussian whose mean velocity and dispersion ($\bar{v_f}$ and σ_f) have been derived by applying the maximum-likelihood technique (equation 3) to stars beyond the cutoff radius. Equation (3) has been then modified to account for the field contamination in the following way:

$$l = \sum_i ln\left(\frac{\exp\left[-\frac{(v_i - \bar{v})^2}{2(\sigma_{\mathrm{LOS}}^2 + \delta_i^2)}\right]}{\sqrt{2\pi(\sigma_{\mathrm{LOS}}^2 + \delta_i^2)}} + \frac{\Gamma_{\mathrm{f}}\exp\left[-\frac{(v_i - \bar{v_f})^2}{2(\sigma_f^2 + \delta_i^2)}\right]}{\Gamma(d_i)\sqrt{2\pi(\sigma_f^2 + \delta_i^2)}}\right), \tag{8}$$

where Γ_{f} is the projected density of field stars. Because of the relatively small area covered by our observations we adopted a constant value of Γ_{f} which has been calibrated to reproduce the fraction of stars within and outside $5\langle\sigma_{\mathrm{LOS}}\rangle$ from the mean systemic velocity and in the radial range between $0.5 < R/r_{\mathrm{t}} < 1$. For each MCMC step, a given combination of k_j parameters is analysed and both the distribution function *f*(*Q*) (using the Eddington 1916 formula; see appendix) and the loglikelihood (from equations 4, 7 and 8) are calculated. At the end of the MCMC cycle, all combinations of k_j producing a negative *f*(*Q*) in any region of the energy domain are rejected and the best-fitting values of k_j are chosen as those where the majority of realizations are placed. The cumulative projected mass profile has been then calculated using equations (4), (5), (6) and

$$M_{\mathrm{dyn}}(R) = 4\pi \int_0^R R' \int_{R'}^{+\infty} \frac{\rho\ r}{\sqrt{r^2 - R'^2}}\mathrm{d}r\ \mathrm{d}R'.$$

Uncertainties in the derived profile have been calculated in a Monte Carlo fashion: for each observed star in the *bona-fide sample*, a synthetic velocity has been extracted from a Gaussian with dispersion equal to the convolution of the best-fitting LOS velocity dispersion at the star distance and its observational uncertainty. The mass profile has been then calculated on the so-obtained synthetic sample using the same procedure adopted for real data. One hundred synthetic samples have been extracted and the rms of the derived masses at different radii have been adopted as uncertainties.

Regarding the anisotropy profile, we considered three cases: isotropic ($\beta = 0$ across the entire cluster extent), a radially anisotropic Osipkov–Merrit profile (Osipkov 1979; Merritt 1985) and a tangentially anisotropic profile. In the considered anisotropic models, the β profile is

$$\beta(r) = \pm\frac{\tilde{r}^2}{1 + \tilde{r}^2}$$

with $\tilde{r} = r/r_{\mathrm{a}}$, where r_{a} is a characteristic radius which sets the boundary where orbits become significantly radially/tangentially biased according to the sign of the right-hand side in the above equation. The choice of these profiles has been made to allow to apply the Eddington (1916) formula even in case of $\beta \neq 0$. The value of r_{a} has been set to the minimum value satisfying the criterion for stability against radial-orbit instability by Nipoti, Londrillo & Ciotti (2002): $\xi_{\mathrm{half}} = 2T_{\mathrm{r}}/T_{\mathrm{t}} < 1.5$ where ξ is the Fridman–Polyachenko–Shukhman parameter (Fridman & Polyachenko 1984), and T_{r} and T_{t} are the radial and tangential component of the kinetic energy tensor calculated within the half-mass radius. In this way, we expect to bracket the entire range of physically meaningful and stable models able to reproduce the structure and kinematics of these two GCs.

The best fits to the projected density and LOS velocity dispersion profiles of the two analysed clusters are shown in Fig. 4.

4 RESULTS

The luminous and dynamical mass profiles of the two analysed GCs within the ACS field of view are shown in Fig. 5. It is apparent that in both clusters dynamical masses are significantly larger than luminous ones across the entire surveyed area. In particular, at a projected distance of 1.6 arcmin (the extent of the ACS field of view) the enclosed dynamical masses are ~3.7 × 10^4 $\mathrm{M}_{\odot}$ and ~3.2 × 10^4 $\mathrm{M}_{\odot}$ in NGC 288 and NGC 6218, respectively, i.e. ~3 times larger than the corresponding luminous masses (~9.3 × 10^3 and ~1.2 × 10^4 $\mathrm{M}_{\odot}$). Although the uncertainties on the dynamical mass estimate are quite large ($\sigma_{\mathrm{M}} \sim 3.8 \times 10^3\ \mathrm{M}_{\odot}$), the above discrepancy stands at a significance of ~6σ. The estimated masses translate into fractions of dark mass within this distance of 75±12 and 62.5±9.6 per cent in NGC 288 and NGC 6218, respectively.

From the mass profiles derived above, it is possible to determine the distribution of dark mass within the area surveyed by our analysis by simply subtracting at each radius the enclosed luminous mass to the dynamical one. The resulting cumulative distribution of dark mass normalized at 1.6 arcmin is compared to those of stars in different mass bins in Fig. 6. For this purpose, we applied equation (1) to stars selected from the photometric data base with

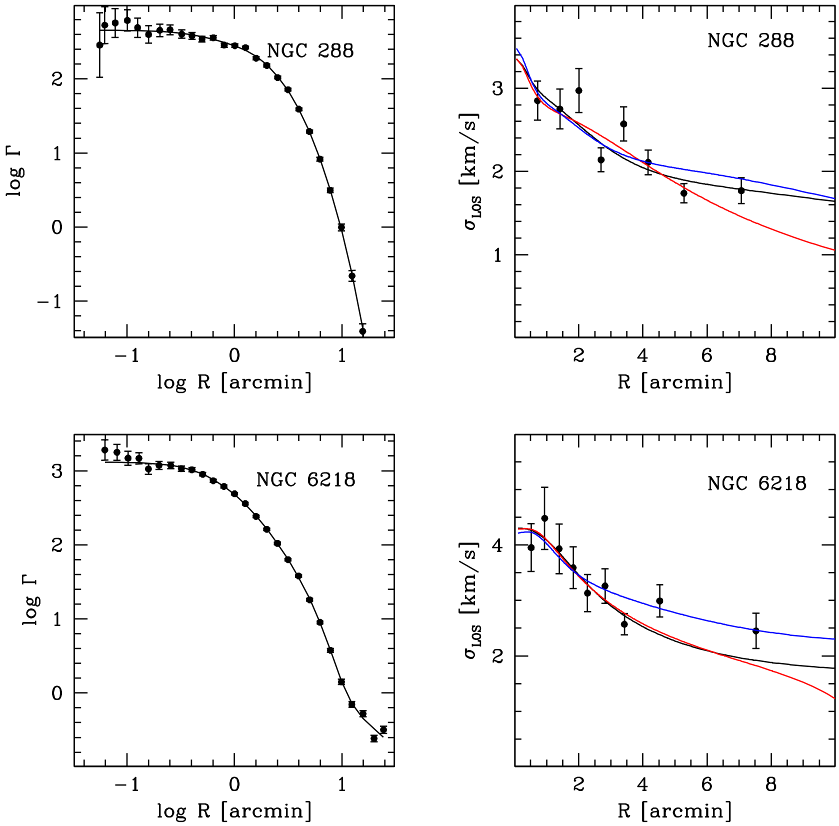

Figure 4. Projected density profiles (left-hand panels) and LOS velocity dispersion profiles (right-hand panels) of NGC 288 (top panels) and NGC 6218 (bottom panels). The best-fitting solution obtained by assuming isotropy, radial and tangential anisotropy are shown as black, red and blue lines (solid, dashed and dot–dashed lines in the printed version of the paper), respectively. The LOS velocity dispersion profiles have been calculated only for illustrative purposes by binning the velocities of the *bona-fide sample* in groups of 50 stars.

mass (derived as described in Section 3.1) comprised in three bins of 0.1 $M_{\odot}$ width. The typical signature of mass segregation is apparent in Fig. 6, with the most massive stars being more concentrated than less massive ones. It is apparent that for both clusters the dark mass is more concentrated than any other mass group. Unfortunately, because of the small number of stars in the innermost pc (i.e. the smallest dispersion of the Gaussian functions adopted to fit the observed profiles; $s_1 = 1$ pc), we are not able to resolve the shape of the dynamical mass density profile within this region (see Section 5).

In the following subsections, we will analyse the possible sources of systematics potentially affecting the above result.

4.1 Possible observational biases

As already discussed in Sollima et al. (2012), the systematics possibly affecting the determination of the luminous mass (like uncertainties on distance, reddening, age, mass–luminosity relation and photometric completeness) have negligible impact unless variations many orders of magnitudes larger than the formal uncertainties are present. In this regard, the dark mass fraction ($f_{\rm dark}$) is less sensitive to the uncertainties in the above assumptions than the M/L ratio. For instance, an incorrect choice of distance (the most uncertain among the above mentioned parameters) would affect both the luminous and dynamical masses in the same direction. Indeed, the luminous mass estimated according to equation (1) depends on the masses of individual stars estimated from their luminosities. Considering that luminosities scale with distance as $L \propto d^2$ and that at low stellar masses $L \propto M^3$, this translates into $M_{\rm lum} \propto d^{2/3}$. On the other hand, the cluster physical radius is proportional to the adopted distance. Following the virial theorem, the same observed velocity dispersion is reproduced by systems with a constant ratio $M_{\rm dyn}/r$, leading to $M_{\rm dyn} \propto d$. So, the luminous-to-dynamical mass ratio has only a small dependence on distance ($M_{\rm lum}/M_{\rm dyn} \propto d^{-1/3}$). Finally, applying the error propagation law one finds

$$\sigma(f_{\rm dark}) = \frac{(1 - f_{\rm dark})}{3} \frac{\sigma(d)}{d}.$$

Considering that GC distances have a typical uncertainty of 5 per cent and that $f_{\rm dark} \sim 65$ per cent this translates into an error of only ∼0.6 per cent in the derived dark mass fraction.

A potentially significant effect can instead be due to the physical processes altering the cluster kinematics. According to equation (2), anisotropy plays a role in shaping the dynamical mass profile. However, as shown in Fig. 5 the derived dynamical mass profile appears to be almost independent on the degree of anisotropy. This is a consequence of the behaviour of the adopted anisotropy profiles which are almost isotropic within the core and deviate from isotropy only outside the area covered by our data. Although the functional form of the anisotropy profile is arbitrary, recent studies based on *HST* proper motion analyses in a wide sample of Galactic GCs, including NGC 288, seem to confirm this trend (Watkins et al. 2015a).

Another source of uncertainty is given by unresolved binaries. Indeed, in a binary system the relative projected velocity of the primary component is added to the motion of the centre of mass,

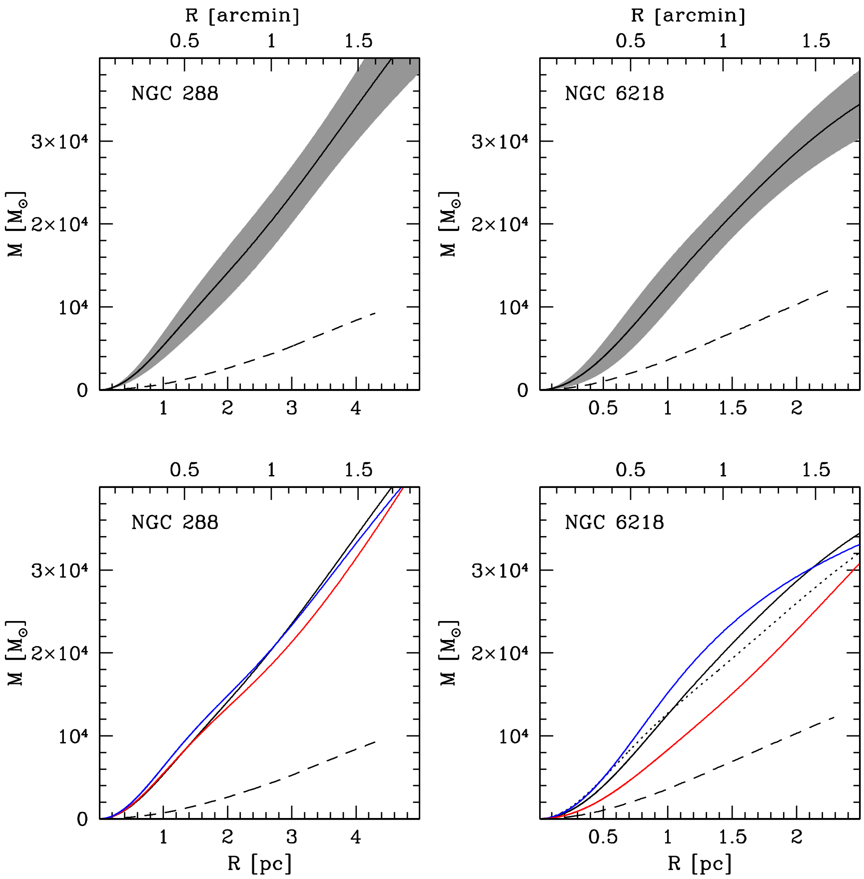

Figure 5. Top panels: cumulative luminous (thick dashed lines) and dynamical (solid lines) mass profiles derived for NGC 288 (left-hand panels) and NGC 6218 (right-hand panels). The 1σ uncertainties about the isotropic model best fit are marked as grey area. Bottom panels: same as top panels where anisotropic fits are shown. The colour code for anisotropic models is the same adopted in Fig. 4. The dotted line in the right-hand panel indicates the dynamical mass profile calculated using only stars with repeated exposures. In all panels, the distance from the cluster centre is reported in both angular (top scale) and physical units (bottom scale).

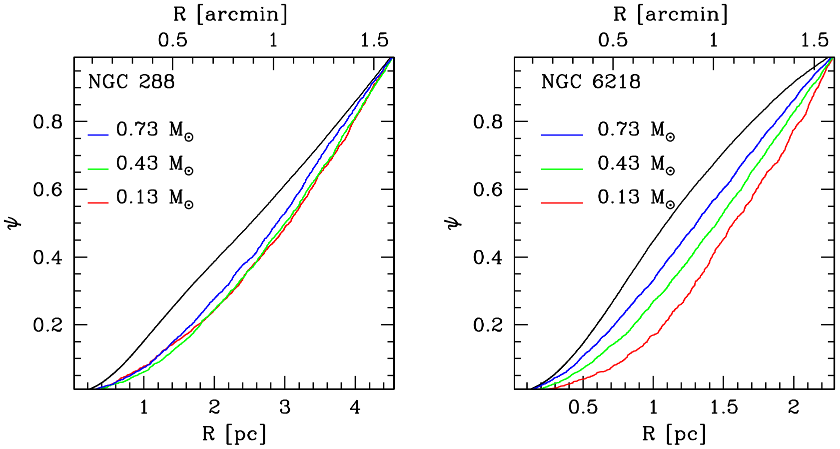

Figure 6. Comparison between the cumulative profile of dark mass (black lines) with those of stars in different mass bins in NGC 288 (left-hand panel) and NGC 6218 (right-hand panel). All profiles are normalized at a distance corresponding to the ACS field of view (1.6 arcmin).

introducing an additional spread in the velocity distribution of the whole population. This effect is maximized in the innermost cluster region where binaries are expected to sink because of their large systemic masses. As explained in Section 2, binaries showing radial velocity variations in multiple data sets have been excluded from the sample. Of course, the binary selection criterion fails for binaries with radial variation amplitude comparable to the observational error. However, in this case the spread produced by undetected binaries would be $<0.3\,\mathrm{km\,s^{-1}}$ producing a negligible effect on the global velocity dispersion in the central region of these clusters. On the other hand, about half of the stars in the *bona-fide sample* are present only in a single data set. For these stars also binaries

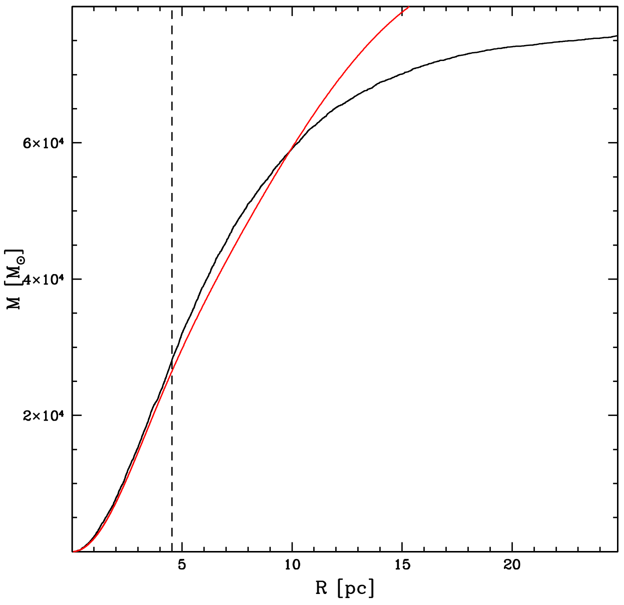

Figure 7. Comparison between the cumulative projected mass profile of the *N*-body simulation of NGC 288 (black line) and that derived from the Jeans analysis (red line; grey in the printed version of the paper). The vertical dashed line indicates the radial extent of this work.

with large radial velocity variations cannot be detected. To test the effect of this contamination, we performed the same analysis using only the binary-cleaned sample of stars with multiple measures for NGC 6218. The resulting mass profile appears to be almost indistinguishable from that derived using the entire *bona-fide sample* (see Fig. 5). So, we conclude that binaries alone cannot produce the observed discrepancy between luminous and dynamical mass. Unfortunately, only few stars with multiple observations are located in the innermost region of NGC 288 thus preventing the application of the same analysis in this cluster.

Finally, the heating due to the tidal interaction of the clusters with the Milky Way can also affect the dynamical mass estimate. Indeed, the periodic shocks occurring every disc crossing and pericentric passage transfer kinetic energy to cluster stars, inflating their velocity dispersion. While this effect is particularly important in the outermost regions (see e.g. Weinberg 1994; Heggie & Hut 2003 and references therein), Küpper et al. (2010) have demonstrated, by means of *N*-body simulations, that a population of potential escapers may have significant effects on the kinematical properties of star clusters, even at intermediate radii. To test this hypothesis, we performed the Jeans analysis on the outcome of the *N*-body simulation run by Sollima et al. (2012) with the orbital and structural characteristics of NGC 288. Particles positions and velocities from the last snapshot of the simulation have been projected into the *x*–*y* plane and a subsample of 450 particles has been randomly extracted. Random velocity offsets extracted from a Gaussian distribution with dispersion equal to 0.5 $\mathrm{km\,s^{-1}}$ have been added to mimic the effect of observational errors. The derived mass profile is compared with the actual mass distribution of the simulation in Fig. 7. It can be seen that the mass distribution is well recovered within 10 per cent at distances $R < 10$ pc (i.e. ∼2.5 times larger than the area covered by our analysis), while at larger distances tidal heating lead to an improper estimate of the enclosed mass. In conclusion, while tidal heating can produce significant effects in the LOS velocity dispersion (see fig. 8 of Sollima et al. 2012) and in the estimate of the enclosed mass outside the half-mass radius of NGC 288, it cannot produce the overabundance of dynamical mass estimated in this paper.

5 EFFECT OF DARK REMNANTS

Since we have ruled out any significant effect of the possible sources of bias in our estimate, the observed discrepancy between luminous and dark mass needs to be interpreted on the basis of physical grounds. As discussed in Section 1, a natural reservoir of non-luminous mass is constituted by dark remnants. In this section, we try to test whether the observed overabundance of mass can be entirely due to these objects.

For this purpose, we analysed three *N*-body simulations selected from the set of Contenta et al. (2015) and compared their fraction of remnants with that measured in NGC 6218. Simulations adopt 131 072 particles extracted from a Kroupa (2001) MF in the mass range $0.1 < M/\mathrm{M}_{\odot} < 15$ and distributed following a King (1966) profile with central adimensional potential $W_0 = 5$ and 7, and a tidal radius equal to the Jacobi radius imposed by the external field. The cluster moves on a circular orbit within a logarithmic potential with circular velocity $v_{\rm circ} = 220\,\mathrm{km\,s^{-1}}$ at a distance of 8.5 kpc from the centre. Simulations were run with NBODY6 (Nitadori & Aarseth 2012) including the effect of stellar evolution with and without the inclusion of natal kicks to NSs. From the entire set of simulations discussed in Contenta et al. (2015), we extracted the snapshot at $t = 13$ Gyr (the age of NGC 6218; Marín-Franch et al. 2009) from simulation 128kN, 12k8N7 and 128kK7. Indeed, the fraction of remnants is highly sensitive to the age of the cluster (see Section 1), and these are the only simulations of the considered data set that survived to dissolution after such time. Simulation 128kN differs from simulations 128kN7 and 128kK7 because of its lower initial concentration ($W_0 = 5$ instead of 7), while simulation 128kK7 assumes natal kicks for NSs, at odds with the other simulations. It is worth stressing that these simulations after 13 Gyr have very different structure, mass, and MF with respect to those of the observed clusters. In particular, their total masses are $<3 \times 10^4\,\mathrm{M}_{\odot}$ (i.e. a factor ∼3 smaller than those of the analysed clusters), and very different projected half-mass radii and MFs. Moreover, the simplified orbits followed by simulations could make them subject to a different tidal stress. Under these conditions, their relaxation time-scales, efficiencies of dark remnant retention and mass-loss rates are likely different from those of the real clusters. On the other hand, in absence of specifically calibrated simulations, this comparison provides a first-order guess of the typical remnant mass fraction and their radial distribution in these stellar systems.

Particle positions have been projected on the *x*–*y* plane and the actual cumulative mass of unevolved stars and remnants have been calculated. Of course, the mass, size and structural properties of the analysed snapshots are substantially different from those of NGC 6218, so to compare the profiles derived from simulations with observations we normalized masses to the total luminous mass and projected distances to the half-mass projected radius of luminous stars ($R_{\rm hm,lum}$). These quantities can be in fact easily calculated in simulations and can be estimated for NGC 6218 from the best-fitting multimass model by Sollima et al. (2012). In Fig. 8, the luminous and total mass profiles of the three analysed snapshots are compared with those observed in the two analysed clusters. Note that while in simulation 128kK7 dark remnants constitute only a small fraction (∼25 per cent) of the total mass within 0.6 $R_{\rm hm,lum}$, in both simulations 128kN and 128kN7 dark remnants represent ∼52 per cent of the total mass within the same radius, only slightly smaller (within 2σ) than those estimated in NGC 288 (75 ± 12 per cent) and

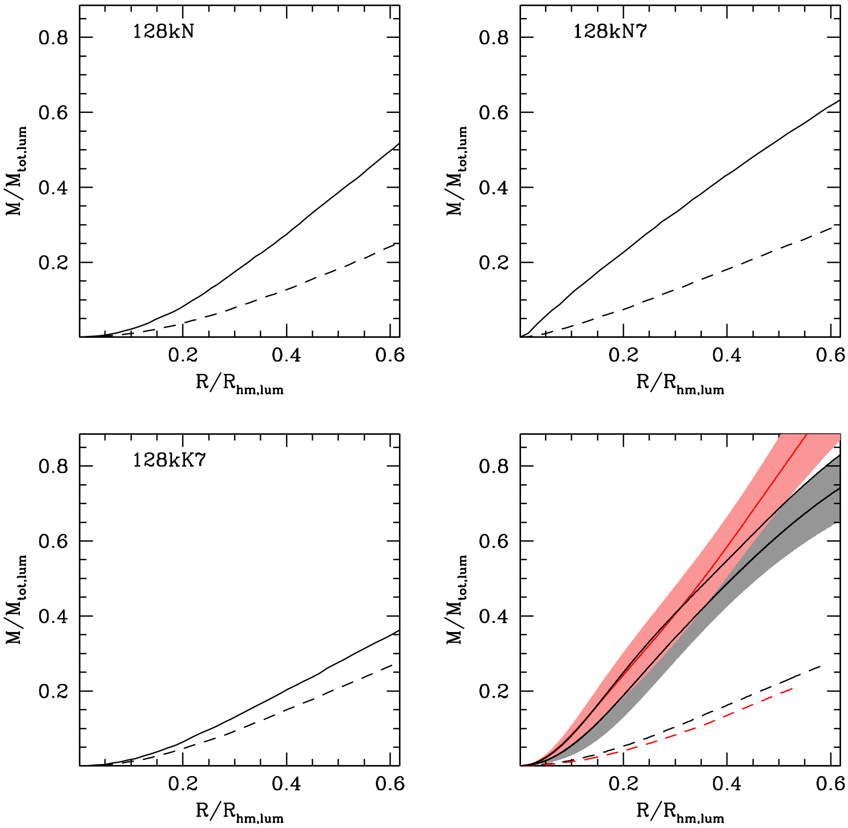

Figure 8. Comparison between the total cumulative mass profile (solid lines) with that of luminous stars (dashed lines) in simulations 128kN (top-left panel), 128kN7 (top-right panel), 128kK7 (bottom-left panel). The luminous and dynamical mass profiles estimated for NGC 288 (red lines, light grey in the printed version of the paper) and NGC 6218 (black lines) are shown in the bottom-right panel with dashed and solid lines, respectively. The shaded area around solid lines indicate the 1σ uncertainty on the dynamical mass profiles. The range in projected distance is the same of Fig. 5

NGC 6218 (62.5 ± 9.7 per cent). It is important to emphasize that even in simulations where natal kicks are not included the large majority of mass in remnants is constituted of WDs (∼87 per cent). So, the large fraction of dark remnants in these simulations is not due to an increased retention of NSs but likely to the role played by the presence of NSs in the initial phase of dynamical evolution of the cluster (see figs 2 and 4 of Contenta et al. 2015). As shown in a number of studies (see e.g. Vesperini & Heggie 1997; Baumgardt & Makino 2003), a significant loss of stars is necessary to explain a large fraction of remnants: the passive evolution of a Kroupa (2001) initial MF in the range $0.1 < M/{\rm M}_{\odot} < 120$ (neglecting dynamically induced losses of stars and NS/BH ejection[3]) would produce a remnant fraction of only ∼28 per cent after 13 Gyr which can only slightly increase as a result of mass segregation of NS, BH and WD progenitors. In this regard, the simulations 128kN, 128kN7 and 128kK7 considered here after 13 Gyr lost 77, 70 and 86 per cent of their initial mass. In this context, estimates of the evaporation rates of these two GCs have been obtained by Kruijssen & Mieske (2009) and Webb & Leigh (2015), providing indications of a significant mass-loss (>80 per cent) in both of them.

In Fig. 9, the cumulative distribution of dark mass normalized at $R/R_{\rm hm,\,lum} = 0.6$ (corresponding to a projected distance of ∼1.6 arcmin in both the GCs analysed in this work) is compared with those of different mass groups in all the considered *N*-body simulations and in NGC 6218, as an example. Qualitatively similar considerations can be made from the comparison with NGC 288 (see Fig. 6). It can be seen that, like in observations, the dark remnant mass is significantly more concentrated than all mass groups in simulation 128kN7, while in other simulations it broadly overlaps the distribution of the most massive luminous stars. This difference likely arises from the larger efficiency of mass segregation in simulation 128kN7 with respect to the other two (see fig. 3 of Contenta et al. 2015). In fact, in this simulation, the difference between the mean mass of WDs and MS stars produces a significant central segregation of the former.

Alternatively, it is also possible that part of the mass excess estimated in the two analysed GCs is concentrated in a single massive remnant located in the cluster centre i.e. an intermediate-mass BH (IMBH). Indeed, the method described in Section 3.2 is not able to resolve density variations within the innermost pc where only a few radial velocities are available. The mass of such an IMBH also depends on the fraction and distribution of other remnants. To test this hypothesis, we adopted the technique described in Sollima et al. (2012) to simultaneously fit the surface brightness profile and the core luminosity function of NGC 6218 with multimass King–Michie models (Gunn & Griffin 1979) with different fractions of dark remnants. A point mass potential has been then added to the model potential to simulate the effect of an IMBH and the LOS

---

[3] This fraction reduces to 24 per cent if a complete ejection of NS and BH is assumed. This can be considered a strong lower limit since all the neglected dynamical processes (retention of NS/BH, central segregation of remnants, preferential loss of low-mass MS stars, etc.) lead to an increase of this fraction.

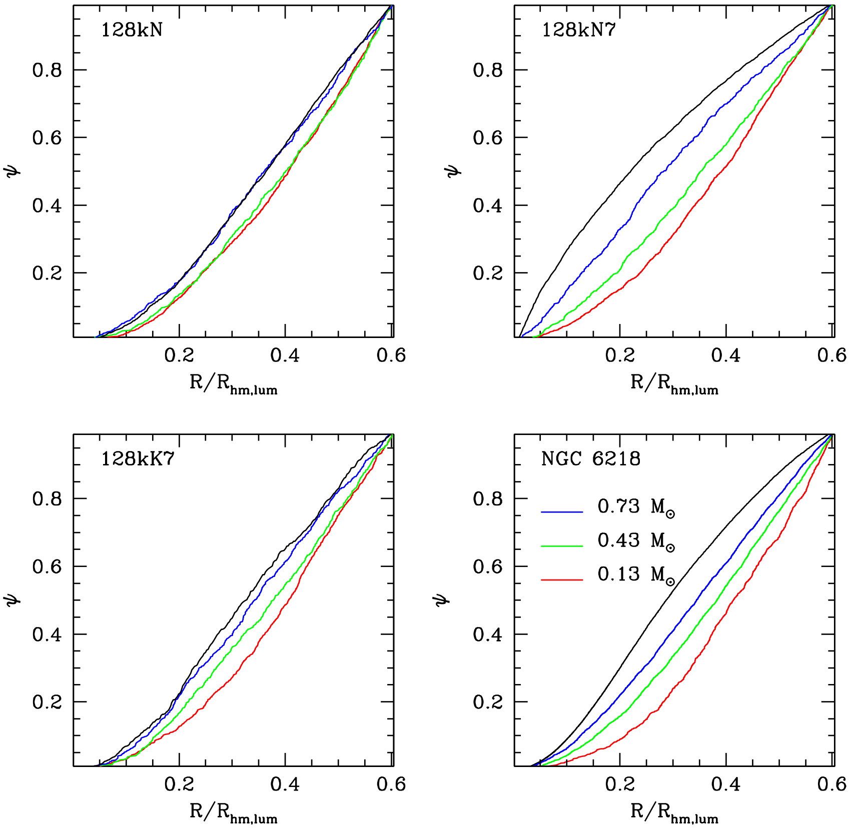

Figure 9. Comparison between the cumulative profile of dark mass (black lines) with those of stars in different mass bins in simulations 128kN (top-left panel), 128kN7 (top-right panel), 128kK7 (bottom-left panel). The profiles estimated for NGC 6218 are shown in the bottom-right panel. All profiles are normalized at a projected distance of $R/R_{\rm hm,\,lum} = 0.6$. The range in projected distance is the same of Fig. 5

velocity dispersion has been derived by integrating equation (2) and using the projection formula in equation (7). Of course, the addition of the point-mass could in principle lead to solutions that are not fully self-consistent. On the other hand, given that $M_{\rm IMBH} \ll M_{\rm dyn}$, this effect is expected to be small and should not affect the following considerations. The best-fitting IMBH mass has been chosen to maximize the loglikelihood (equation 8). In Fig. 10, the best-fitting IMBH mass is plotted as a function of the adopted remnants global mass fraction. As expected, the larger is the fraction of remnants ($f_{\rm remn}$) the smaller is the mass of the hypothetical IMBH. Note that for any dark remnants mass fraction >24 per cent (a strong lower limit according to the considerations made above), the IMBH mass is always $<7 \times 10^3$ M$_\odot$ while for $f_{\rm remn} > 52$ per cent no IMBH are allowed.

6 SUMMARY

The main result obtained in this paper is that the largest fraction (>60 per cent) of the mass content of both the analysed GCs is dominated by centrally concentrated non-luminous mass.

The results presented here confirm what already found in Sollima et al. (2012). However, a significant improvement with respect to that work has been made here since: (i) the adopted data set of radial velocities is ∼5 times larger within the half-light radii of both clusters, (ii) the analysis presented here is model-independent as it requires no assumptions on the degree of mass segregation among mass groups, and (iii) in this work we are able to determine the radial distribution of the dark mass.

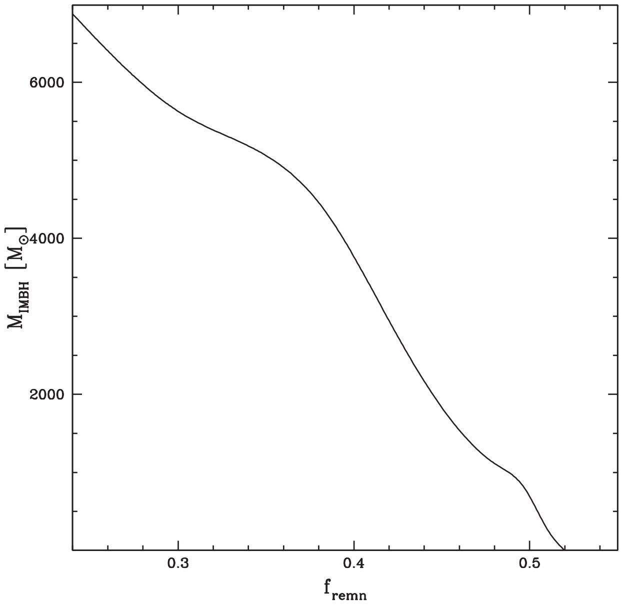

Figure 10. Best-fitting IMBH mass in NGC 6218 as a function of the adopted global mass fraction of dark remnants.

The obtained result seems not to be due to the heating produced by tidal effects or binary stars being therefore linked to a real excess of dark mass in the central region of these clusters.

The most likely hypothesis is that such a large mass excess is produced by dark remnants sunk in the cluster core during the cluster lifetime as a result of mass segregation. In fact, the comparison with *N*-body simulations indicates that GCs losing a significant (>70 per cent) fraction of their initial mass contain a centrally concentrated core of dark remnants constituted mainly of WDs accounting for ∼50 per cent of the total cluster mass within the same radial extent explored in the present analysis. This value is slightly lower, but within the uncertainties, than that estimated in our analysis. It is worth noting that the *N*-body simulations considered in this work were not specifically run to reproduce the present-day structure of the two analysed clusters and are subject to a different tidal stress. So, only qualitative conclusions can be drawn from such a comparison. However, similar results are obtained by other authors: Giersz & Heggie (2011) used Monte Carlo simulations with 2×10^6 particles to model the present-day structure of 47 Tuc and found that the fraction of WDs is ∼51 per cent in the core and even larger in a scaled simulation run with a flatter initial MF. Sippel et al. (2012) and Lützgendorf et al. (2013) analysed a set of *N*-body simulations including natal kicks for NSs and BHs and found that after 12 Gyr ∼40 per cent of the cluster mass is contained in WDs (and a larger fraction is expected in the core). According to Vesperini & Heggie (1997) and Baumgardt & Makino (2003), the fraction of WDs and NSs steadily increases as a cluster evolves and loses mass, becoming dominant when the cluster lost >60 per cent of its stars. In this regard, a large mass-loss rate in the two analysed clusters is also suggested by their relatively flat MFs (de Marchi, Pulone & Paresce 2006; Paust et al. 2010; Sollima et al. 2012). On the basis of the above consideration, it is still possible that the observed overabundance of non-luminous mass in the two GCs analysed here is entirely due to a compact population of centrally segregated WDs. A valuable test to this hypothesis would be to measure the number of WDs in the central region of these clusters through photometric analyses. Unfortunately, to perform a complete census of WDs in these clusters it would be necessary to reach extremely faint magnitudes ($V \sim 30$–31) with a good level of completeness, an unfeasible task even with *HST*.

The possible presence of an IMBH in the centre of these two GCs, as suggested for many other Galactic GCs by Lützgendorf et al. (2013; but see van der Marel & Anderson 2010; Lanzoni et al. 2013), cannot be excluded. In particular, according to the actual fraction of retained remnants, the mass of such an hypothetical BH could lie in the range $M_{\rm IMBH} < 7 \times 10^3\,{\rm M}_{\odot}$. On the other hand, we believe that given the above apparent degeneracy and the large uncertainty in the expected dark remnants fractions, any claim of IMBH detection is inappropriate. Similarly, the presence of an IMBH can significantly affect the determination of the actual fraction of remnants.

Another possibility is that the mass excess observed here is due to a modest amount of non-baryonic DM. Previous investigations in this regard made on the outer halo GC NGC 2419 seem to rule out the presence of a significant amount of DM within the stellar extent of this cluster (Baumgardt et al. 2009; Conroy, Loeb & Spergel 2011) although the involved uncertainties in the anisotropy profile leave some room for a small DM content (Ibata et al. 2013). Note that in this scenario the DM halo should extend far beyond the extent of the stellar component. *N*-body simulations assuming GCs surrounded by cored DM haloes predict that, because of the interaction with the cluster stars (Baumgardt & Mieske 2008) and stripping by the tidal field of the host galaxy, the central parts of GCs might be left relatively poor in DM because at the present time the DM either populates the outer region of the cluster or has been stripped (Mashchenko & Sills 2005; Peñarrubia, Navarro & McConnachie 2008). In this scenario, the high concentration of dark mass evidenced in our analysis would favour a cuspy shape of the surviving DM halo dominating the cluster mass budget in the central region of these clusters. This is however in contrast with theoretical considerations (where interactions with baryons are expected to remove DM cusps; Navarro, Eke & Frenk 1996; Mo & Mao 2004; Mashchenko, Couchman & Wadsley 2006; Del Popolo 2009; Di Cintio et al. 2014; Pontzen & Governato 2014; Nipoti & Binney 2015).

Because of the limited sample of GCs analysed here, it is not possible to check the presence of correlation between dark mass content and other dynamical and general parameters. Future studies addressed to the extension of this analysis to a larger sample of GCs will help to clarify the nature of the dark mass and the effect of the various dynamical processes occurring during the cluster evolution on its fraction.

ACKNOWLEDGEMENTS

AS acknowledges the PRIN INAF 2011 ‘Multiple populations in GCs: their role in the Galaxy assembly’ (PI Carretta) and the PRIN INAF 2014 ‘Probing the internal dynamics of GCs. The first, comprehensive radial mapping of individual star kinematics with the generation of multi-object spectrographs’ (PI Origlia). AS, FRF, EL, BL, AM, ED and CP acknowledge support from the European Research Council (ERC-2010-AdG-267675, COSMIC-LAB). FC acknowledge support from the European Research Council (ERCStG-335936, CLUSTERS). We warmly thank Michele Bellazzini, Yazan Momany, Anna Lisa Varri and Douglas Heggie for useful discussions and suggestions. We also thank the anonymous referee whose helpful comments and suggestions improved our paper. Based on FLAMES observations collected with the Very Large Telescope of the ESO, Cerro Paranal, Chile, within the observing programmes 68.D-0212, 69.D-0582, 071.D-0131, 073.D-0211, 074.A-0508, 075.D-0043, 087.D-0276, 088.B-0403, 193.B-0936 and 193.D-0232 and on observations made with the NASA/ESA *HST*, which is operated by the association of Universities for Research in Astronomy, Inc., under the NASA contract NAS 5-26555, under programmes GO-10775 (PI: Sarajedini).

REFERENCES

Anderson J. et al., 2008, AJ, 135, 2055
Banerjee S., Kroupa P., 2011, ApJ, 741, L12
Bastian N., Covey K. R., Meyer M. R., 2010, ARA&A, 48, 339
Baumgardt H., Makino J., 2003, MNRAS, 340, 227
Baumgardt H., Mieske S., 2008, MNRAS, 391, 942
Baumgardt H., Côté P., Hilker M., Rejkuba M., Mieske S., Djorgovski S. G., Stetson P., 2009, MNRAS, 396, 2051
Bellazzini M., Fusi Pecci F., Messineo M., Monaco L., Rood R. T., 2002, AJ, 123, 1509
Bellazzini M., Bragaglia A., Carretta E., Gratton R. G., Lucatello S., Catanzaro G., Leone F., 2012, A&A, 538, A18
Breen P. G., Heggie D. C., 2013, MNRAS, 432, 2779
Bruzual G., Charlot S., 2003, MNRAS, 344, 1000
Cappellari M., 2002, MNRAS, 333, 400
Chomiuk L., Strader J., Maccarone T. J., Miller-Jones J. C. A., Heinke C., Noyola E., Seth A. C., Ransom S., 2013, ApJ, 777, 69
Clark G. W., 1975, ApJ, 199, L143
Conroy C., Loeb A., Spergel D. N., 2011, ApJ, 741, 72
Contenta F., Varri A. L., Heggie D. C., 2015, MNRAS, 449, L100
de Marchi G., Pulone L., Paresce F., 2006, A&A, 449, 161
Del Popolo A., 2009, ApJ, 698, 2093

Di Cintio A., Brook C. B., Macciò A. V., Stinson G. S., Knebe A., Dutton A. A., Wadsley J., 2014, MNRAS, 437, 415

Dirsch B., Richtler T., 1995, A&A, 303, 742

Dotter A., Chaboyer B., Jevremović D., Baron E., Ferguson J. W., Sarajedini A., Anderson J., 2007, AJ, 134, 376

Dotter A. et al., 2010, ApJ, 708, 698

Drukier G. A., 1996, MNRAS, 280, 498

Eddington A. S., 1916, MNRAS, 76, 572

Fridman A. M., Polyachenko V. L., 1984, Physics of Gravitating Systems – II, Nonlinear Collective Processes: Nonlinear Waves, Solitons, Collisionless Shocks, Turbulence. Springer-Verlag, New York

Gebhardt K., Fischer P., 1995, AJ, 109, 209

Giersz M., Heggie D. C., 2011, MNRAS, 410, 2698

Grindlay J. E., Bailyn C. D., 1988, Nature, 336, 48

Gunn J. E., Griffin R. F., 1979, AJ, 84, 752

Harris W. E., 1996, AJ, 112, 1487

Heggie D. C., Giersz M., 2014, MNRAS, 439, 2459

Heggie D. C., Hut P., 1996, in Hut P., Makino J., eds, Proc. IAU Symp. 174, White Dwarfs. Kluwer, Dordrecht, p. 303

Heggie D. C., Hut P., 2003, The Gravitational Million-Body Problem: A Multidisciplinary Approach to Star Cluster Dynamics. Cambridge Univ. Press, Cambridge

Heyl J., Richer H. B., Antolini E., Goldsbury R., Kalirai J., Parada J., Tremblay P.-E., 2015, ApJ, 804, 53

Ibata R., Nipoti C., Sollima A., Bellazzini M., Chapman S. C., Dalessandro E., 2013, MNRAS, 428, 3648

Kalirai J. S., Hansen B. M. S., Kelson D. D., Reitzel D. B., Rich R. M., Richer H. B., 2008, ApJ, 676, 594

Kamann S., Wisotzki L., Roth M. M., Gerssen J., Husser T.-O., Sandin C., Weilbacher P., 2014, A&A, 566, A58

King I. R., 1966, AJ, 71, 64

Kroupa P., 2001, MNRAS, 322, 231

Kruijssen J. M. D., 2015, MNRAS, 454, 1658

Kruijssen J. M. D., Mieske S., 2009, A&A, 500, 785

Kulkarni S. R., Hut P., McMillan S., 1993, Nature, 364, 421

Küpper A. H. W., Kroupa P., Baumgardt H., Heggie D. C., 2010, MNRAS, 407, 2241

Lane R. R. et al., 2010, MNRAS, 406, 2732

Lane R. R., Kiss L. L., Lewis G. F., Ibata R. A., Siebert A., Bedding T. R., Székely P., Szabó G. M., 2011, A&A, 530, A31

Lanzoni B. et al., 2013, ApJ, 769, 107

Leonard P. J. T., Richer H. B., Fahlman G. G., 1992, AJ, 104, 2104

Lucatello S., Tsangarides S., Beers T. C., Carretta E., Gratton R. G., Ryan S. G., 2005, ApJ, 625, 825

Lucatello S., Sollima A., Gratton R., Vesperini E., D'Orazi V., Carretta E., Bragaglia A., 2015, A&A, 584, A52

Lützgendorf N. et al., 2013, A&A, 552, A49

Lützgendorf N., Baumgardt H., Kruijssen J. M. D., 2013, A&A, 558, A117

McLaughlin D. E., van der Marel R. P., 2005, ApJS, 161, 304

Marín-Franch A. et al., 2009, ApJ, 694, 1498

Mashchenko S., Sills A., 2005, ApJ, 619, 258

Mashchenko S., Couchman H. M. P., Wadsley J., 2006, Nature, 442, 539

Merritt D., 1985, AJ, 90, 1027

Meylan G., Mayor M., 1991, A&A, 250, 113

Miller-Jones J. C. A. et al., 2015, MNRAS, 453, 3918

Milone A. P. et al., 2012, A&A, 540, A16

Miocchi P. et al., 2013, ApJ, 774, 151

Mo H. J., Mao S., 2004, MNRAS, 353, 829

Moody K., Sigurdsson S., 2009, ApJ, 690, 1370

Morscher M., Umbreit S., Farr W. M., Rasio F. A., 2013, ApJ, 763, L15

Morscher M., Pattabiraman B., Rodriguez C., Rasio F. A., Umbreit S., 2015, ApJ, 800, 9

Navarro J. F., Eke V. R., Frenk C. S., 1996, MNRAS, 283, L72

Nipoti C., Binney J., 2015, MNRAS, 446, 1820

Nipoti C., Londrillo P., Ciotti L., 2002, MNRAS, 332, 901

Nitadori K., Aarseth S. J., 2012, MNRAS, 424, 545

Osipkov L. P., 1979, Pisma Astron. Zh., 5, 77

Pasquini L. et al., 2002, The Messenger, 110, 1

Paust N. E. Q. et al., 2010, AJ, 139, 476

Peebles P. J. E., 1984, ApJ, 277, 470

Peñarrubia J., Navarro J. F., McConnachie A. W., 2008, ApJ, 673, 226

Piatek S., Pryor C., McClure R. D., Fletcher J. M., Hesser J. E., 1994, AJ, 107, 1397

Pontzen A., Governato F., 2014, Nature, 506, 171

Richer H. B., Fahlman G. G., 1989, ApJ, 339, 178

Robin A. C., Reylé C., Derrière S., Picaud S., 2003, A&A, 409, 523

Sarajedini A. et al., 2007, AJ, 133, 1658

Shanahan R. L., Gieles M., 2015, MNRAS, 448, L94

Sigurdsson S., Hernquist L., 1993, Nature, 364, 423

Sippel A. C., Hurley J. R., 2013, MNRAS, 430, L30

Sippel A. C., Hurley J. R., Madrid J. P., Harris W. E., 2012, MNRAS, 427, 167

Skrutskie M. F. et al., 2006, AJ, 131, 1163

Sollima A., Beccari G., Ferraro F. R., Fusi Pecci F., Sarajedini A., 2007, MNRAS, 380, 781

Sollima A., Bellazzini M., Lee J.-W., 2012, ApJ, 755, 156

Sollima A., Baumgardt H., Zocchi A., Balbinot E., Gieles M., Hénault-Brunet V., Varri A. L., 2015, MNRAS, 451, 2185

Spitzer L., Jr, 1969, ApJ, 158, L139

Stetson P. B., 1994, PASP, 106, 250

Strader J., Caldwell N., Seth A. C., 2011, AJ, 142, 8

Strader J., Chomiuk L., Maccarone T. J., Miller-Jones J. C. A., Seth A. C., 2012, Nature, 490, 71

Taylor M. A., Puzia T. H., Gomez M., Woodley K. A., 2015, ApJ, 805, 65

Tollerud E. J., Bullock J. S., Graves G. J., Wolf J., 2011, ApJ, 726, 108

Tolstoy E., Hill V., Tosi M., 2009, ARA&A, 47, 371

Trager S. C., King I. R., Djorgovski S., 1995, AJ, 109, 218

van der Marel R. P., Anderson J., 2010, ApJ, 710, 1063

Vesperini E., Heggie D. C., 1997, MNRAS, 289, 898

Watkins L. L., van der Marel R. P., Bellini A., Anderson J., 2015a, ApJ, 803, 29

Watkins L. L., van der Marel R. P., Bellini A., Anderson J., 2015b, ApJ, 812, 149

Webb J. J., Leigh N. W. C., 2015, MNRAS, 453, 3278

Weinberg M. D., 1994, AJ, 108, 1414

White S. D. M., Rees M. J., 1978, MNRAS, 183, 341

APPENDIX: DISTRIBUTION FUNCTION FROM MULTIGAUSSIAN EXPANSION OF DENSITY AND VELOCITY DISPERSION PROFILES

According to Eddington (1916), the distribution function of a spherical and isotropic system can be derived from the formula

$$
\begin{aligned}
f(E) &= -\frac{1}{\sqrt{8}\pi}\left[\int_E^{\phi_\mathrm{t}} \frac{\mathrm{d}^2\rho}{\mathrm{d}\phi^2}\frac{\mathrm{d}\phi}{\sqrt{\phi-E}} - \frac{1}{\sqrt{\phi_t - E}}\left(\frac{\mathrm{d}\rho}{\mathrm{d}\phi}\right)_{\phi=\phi_\mathrm{t}}\right]\\
&= -\frac{1}{\sqrt{8}\pi}\left[G\int_{r(\phi=E)}^{r_\mathrm{t}} \frac{\mathrm{d}^2\rho}{\mathrm{d}\phi^2}\frac{M(r)}{r^2\sqrt{\phi(r)-E}}\mathrm{d}r\right.\\
&\qquad \left. - \frac{1}{\sqrt{\phi_\mathrm{t} - E}}\left(\frac{\mathrm{d}\rho}{\mathrm{d}\phi}\right)_{\phi=\phi_\mathrm{t}}\right], \qquad \text{(A1)}
\end{aligned}
$$

where $\phi_\mathrm{t} = -GM/r_\mathrm{t}$ is the potential at the cluster tidal radius. The above equation can be generalized to account for Osipkov–Merritt anisotropic models by replacing E with

$$Q \equiv \phi_\mathrm{t} - E - L^2/2r_\mathrm{a}^2$$

and ρ with

$$\rho_Q \equiv (1+\tilde{r}^2)\rho.$$

Any physically meaningful model must satisfy the inequality $f(Q) > 0$ across the entire range of Q.

All the terms in equation (A1) can be written as a function of the 3D mass, global density profile (equation 6) and its radial derivatives.

$$\frac{\mathrm{d}\rho_Q}{\mathrm{d}\phi} = \frac{r}{GM(r)}\left[r(1+\tilde{r}^2)\frac{\mathrm{d}\rho}{\mathrm{d}r} + 2\rho\tilde{r}^2\right]$$

$$\frac{\mathrm{d}^2\rho_Q}{\mathrm{d}\phi^2} = \left(\frac{r}{GM(r)}\right)^2\left[r^2(1+\tilde{r}^2)\frac{\mathrm{d}^2\rho}{\mathrm{d}r^2} + 2r(1+3\tilde{r}^2)\frac{\mathrm{d}\rho}{\mathrm{d}r} - \frac{4\pi\rho r^4}{M(r)}(1+\tilde{r}^2)\frac{\mathrm{d}\rho}{\mathrm{d}r} + 2\rho\tilde{r}^2\left(3 - \frac{4\pi\rho r^3}{M(r)}\right)\right]$$

$$\phi(r) = -G\left[\frac{M(r)}{r} + 4\pi\int_r^{r_t}\rho\, r\, \mathrm{d}r\right].$$

So, the distribution function *f*(Q) can be derived by numerically integrating equation (A1) for each value of Q in the range $\phi(0) < Q < \phi_{\mathrm{t}}$.

This paper has been typeset from a TEX/LATEX file prepared by the author.